Confinedness of an X3.1-class Solar Flare Occurred in NOAA 12192: Analysis from Multi-instrument Observations

N. Vasantharaju[1] , F. Zuccarello[1,2] , F. Ferrente[1], and S. L. Guglielmino[2]

[1] Department of Physics and Astronomy "Ettore Majorana," Università degli Studi di Catania, Via S. Sofia 78, I-95123 Catania, Italy
vasantharaju.naganna@dfa.unict.it

[2] INAF—Catania Astrophysical Observatory, Via S. Sofia 78, I-95123 Catania, Italy

Abstract

The nonassociation of coronal mass ejections with high energetic flares is sparse. For this reason, the magnetic conditions required for the confinedness of major flares is a topic of active research. Using multi-instrument observations, we investigated the evolution and effects of confinedness in an X3.1 flare, which occurred in active region (AR) 12192. The decrease of net fluxes in the brightening regions near the footpoints of the multisigmoidal AR in the photosphere and chromosphere, indicative of flux cancellation favoring tether-cutting reconnection (TCR), is observed using the magnetic field observations of HMI/SDO and SOT/Hinode, respectively. The analysis of spectropolarimetric data obtained by the Interferometric Bidimensional Spectrometer over the brightening regions suggests untwisting of field lines, which further supports TCR. Filaments near the polarity inversion line region, resulting from TCR of low-lying sheared loops, undergo merging and form an elongated filament. The temperature and density differences between the footpoints of the merged filament, revealed by DEM analysis, cause streaming and counterstreaming of the plasma flow along the filament and unload at its footpoints with an average velocity of ≈ 40 km s^{-1}. This results in a decrease of the mass of the filament (density decreased by $>50\%$), leading to its rise and expansion outward. However, due to strong strapping flux, the filament separates itself instead of erupting. Further, the evolution of nonpotential parameters describes the characteristics of confinedness of the flare. Our study suggests that the sigmoid–filament system exhibits upward catastrophe due to mass unloading but gets suppressed by strong confinement of the external poloidal field.

Unified Astronomy Thesaurus concepts: Solar active regions (1974); Solar active region magnetic fields (1975); Solar activity (1475); Solar active region filaments (1977); Solar flares (1496)

Supporting material: animation

1. Introduction

Solar flares and coronal mass ejections (CMEs) are violent explosive phenomena that occur on the Sun. If both of these phenomena occur simultaneously and are directed at Earth, they can produce detrimental effects on Earth's magnetosphere and atmosphere. The active regions (ARs) with high magnetic complexity and nonpotentiality produce these explosive phenomena (Zirin & Liggett 1987; Schrijver et al. 2005), and when flares are accompanied by CMEs they are referred to as eruptive or else confined/noneruptive. The association of flares and CMEs has been studied quite extensively and is still an active research topic. Previous findings, for example, Yashiro et al. (2006), showed that the probability of a CME–flare association rate increases with the increase in flare strength, and the association rate is 90%–92% for X3.0-class or more intense flares.

The magnetic flux ropes (MFRs), twisted magnetic field lines wrapped around the axial magnetic field, are an essential part of CME structure and support filament/prominence plasma against gravity. There are many possible mechanisms responsible for initiating the outward motion of the MFR, and they all come under three main models: ideal magnetohydrodynamic (MHD) instabilities (Török & Kliem 2003), flux rope

catastrophes (van Tend & Kuperus 1978), and magnetic reconnection (Antiochos et al. 1999; Moore et al. 2001). One popular mechanism in the context of ideal MHD instability is helical kink instability (Török et al. 2004). Kink instability triggers when the twist of the MFR exceeds the critical twist value of 2.5π (Török & Kliem 2003). Another mechanism relevant to the present study in the context of MFR catastrophe is the "mass draining" or "mass unloading" effect, which perturbs the equilibrium of the MFR. In this mechanism, an upward catastrophe occurs when the mass of the MFR decreases below a critical value (Jenkins et al. 2019; Zhang et al. 2021). Under the magnetic reconnection models, the tether-cutting reconnection (Moore et al. 2001) between sheared arcades can explain the formation and initiation of MFR eruption successfully. Though these mechanisms efficiently explain the initiation of the rising motion of the MFR, they fail to explain confined or suppressed eruptions after the MFR exceeds the critical values. For example, a statistical study (Jing et al. 2018) of 36 strong flare events shows that kink instability plays a minor role in the successful eruption of MFRs. Thus, the rate at which the overlying magnetic field decays with height plays an important role in determining the confinedness or successful eruption of the MFR. This kind of ideal MHD instability is known as torus instability (TI; Bateman 1978; Kliem & Török 2006). The TI triggers when there is a force imbalance between the outward "hoop force" due to the curvature of the MFR and the inwardly directed Lorentz force due to the overlying field. It is quantified by a

dimensionless parameter, the decay index n, which indicates the rate at which the overlying field declines with height. The MHD simulations provide the onset TI criterion when $n \geqslant 1.5$ (Török & Kliem 2005). In some events, even torus-unstable ($n > 1.5$) flux ropes fail to erupt, and studies were conducted in this direction as well in determining the causes for the confinedness of such events. A few notable ones are the dynamic tension force from the external toroidal field (Myers et al. 2015), the Lorentz force due to the nonaxisymmetry of the flux rope (Zhong et al. 2021), and the rotation of the flux rope (Zhou et al. 2019), all of which could contribute to the downward Lorentz force in confining the eruption.

Andrews (2003) showed that about 40% of the M-class flares that occurred during the period 1996–1999 are confined and that there is a high probability of a lack of CMEs associated with weaker flares (less than C-class), whereas confined eruptions with more energetic flares are rare. Schmahl et al. (1990) reported a confined X4-class flare that occurred in AR 4492 on 1984 May 19 using radio and X-ray observations. A few more case studies of X-class confined flares were done by Feynman & Hundhausen (1994), Green et al. (2002), Chen et al. (2013), and Liu et al. (2014). Wang & Zhang (2007) conducted a statistical study of 104 X-class flares during 1996–2004 and showed that confined X-class flares, constituting 10% of the sample, occur closer to the AR center, while the eruptive flares are at the outskirts. Cheng et al. (2011) performed a comparative study between eruptive (three) and confined (six) flares that occurred in AR 10720 and found that the eruptive flares have a higher decay index in the low corona ($<$10 Mm) than the confined ones.

The AR 12192 is one of the largest, flare-prolific and CME-poor ARs of solar cycle 24. This AR produced about 35 major noneruptive flares (29 M-class and 6 X-class) and one eruptive flare (M4.0) during its disk passage from 2014 October 18 to 29. Many studies were conducted on the X3.1 confined flare event, the strongest among the flare series. Sun et al. (2015) and Sarkar & Srivastava (2018) studied the magnetic conditions of the AR and found that the core of the AR exhibits weak nonpotentiality and small flare-related field changes and attributed the strong overlying magnetic field strength to the confined nature of the flare. Using nonlinear force-free field extrapolations, Inoue et al. (2016) showed that the core of AR 12192 is a multiflux tube system located near the polarity inversion line (PIL) region, where the onset of the flare is due to the tether-cutting reconnection of the low-lying field lines of the multiflux tube system. The confinedness of the eruption is attributed to low sheared field lines, which are kink-stable, as well as to the strong overlying field strength. Using simulations, Jiang et al. (2016) suggested that the absence of the flux rope resulted in the confined eruption. On the contrary, Zhang et al. (2017) suggested that that confined flare was due to the complexity of the magnetic field structures.

Past observational and simulation studies could successfully explain the formation of a postflare, less sheared core field and stableness against kink instability, but they did not explain the formation of the observed filament and its rising motion during the long-duration X3.1 flare event. Owing to the peculiar qualities and rareness of the event, we carried out a comprehensive analysis to investigate the evolution, cause, and properties of the confinedness of the X3.1 flare using spectropolarimetric imaging data, magnetograms, and filtergrams corresponding to different layers of the solar atmosphere obtained by multiple instruments on board different space- and ground-based telescopes. A description of the instruments and data is provided in Section 2. In Section 3, we detail the analysis and results, followed by a summary and discussion in Section 4.

2. Observations and Data

The high spatial, temporal, and spectral resolution spectro-polarimetric data in the Ca II 8542 Å line, used in the present analysis, were obtained by the Interferometric Bidimensional Spectrometer (IBIS; Cavallini & Reardon 2006; Reardon & Cavallini 2008) at the ground-based Dunn Solar Telescope (DST). The IBIS instrument is based on a dual Fabry–Perot interferometer and mounted in the collimated beam of DST. The Ca II 8542 Å line was scanned along 25 wavelength points from 8539.8 to 8544.6 Å, with an average step size of 0.19 Å. The pixel size is $0''095$, and the maximum spatial resolution is about $0''3$. There are two sets of observations available, corresponding to two different fields of view (FOVs) over AR 12192, with a total of 144 full spectropolarimetric scans on 2014 October 24. These two sets of observations track portions of flare ribbon evolution corresponding to two different flares that occurred in AR 12192 on 2014 October 24. The FOV for the first set of observations corresponds to a C5.1 flare (start time, 14:31 UT; peak time, 15:06 UT; end time, 15:54 UT). For this flare, we have IBIS observations from 14:55 to 16:42 UT (indicated by the light green shaded region in Figure 1(a)) and not used in the present work. The FOV for the second set of observations corresponds to the X3.1 flare (start time, 21:07 UT; peak time, 21:41 UT; end time, 22:13 UT). For this flare, we have IBIS observations from 21:20 to 22:30 UT. This FOV is marked as a red dashed rectangle in Figure 1(b). Unfortunately, due to poor seeing conditions, we could not use the entire data set acquired during this time period. Based on the rms contrast and visual inspection, we selected only six good scans of IBIS data included in the time interval indicated by the dark green shaded region in Figure 1(a).

The Solar Optical Telescope (SOT; Ichimoto et al. 2008; Tsuneta et al. 2008) on board Hinode has two filtergraph instruments called the Broadband Filter Imager (BFI) and the Narrowband Filter Imager (NFI), as well as a spectropolarimeter (SP). We used filtergrams obtained by the BFI in the Ca II H line (3968 Å) and Stokes V/I images obtained by NFI in the Na I D1 line (5896 Å). The Ca II H and Na I D1 lines are sensitive to the upper and lower chromosphere, respectively. The FOV of SOT was limited to $328'' \times 164''$ for the NFI and $218'' \times 109''$ for the BFI. The blue dashed rectangle in Figure 1(b) marks the FOV of the Hinode filtergraph observations used in the present study. The spatial resolutions of the NFI and BFI are about $0''3$ and $0''2$, respectively. To calibrate Na I D1 V/I data, we used the B_{LOS} magnetogram derived from the level 2 data set of SP.

The Hα data acquired from six different telescopes of the Global Oscillation Network Group (GONG; Harvey et al. 2011) were used in the analysis of filament evolution during the decay phase of the X3.1 flare. GONG provides full-disk Hα images at a cadence of 1 minute with a pixel size of $1''$.

The Atmospheric Imaging Assembly (AIA; Lemen et al. 2012) on board the Solar Dynamics Observatory (SDO; Pesnell et al. 2012) produces full-disk extreme-ultraviolet (EUV) images in 10 wavelength bands at a high cadence of 12 s with a pixel size of $0''6$. The photospheric magnetic field observations are
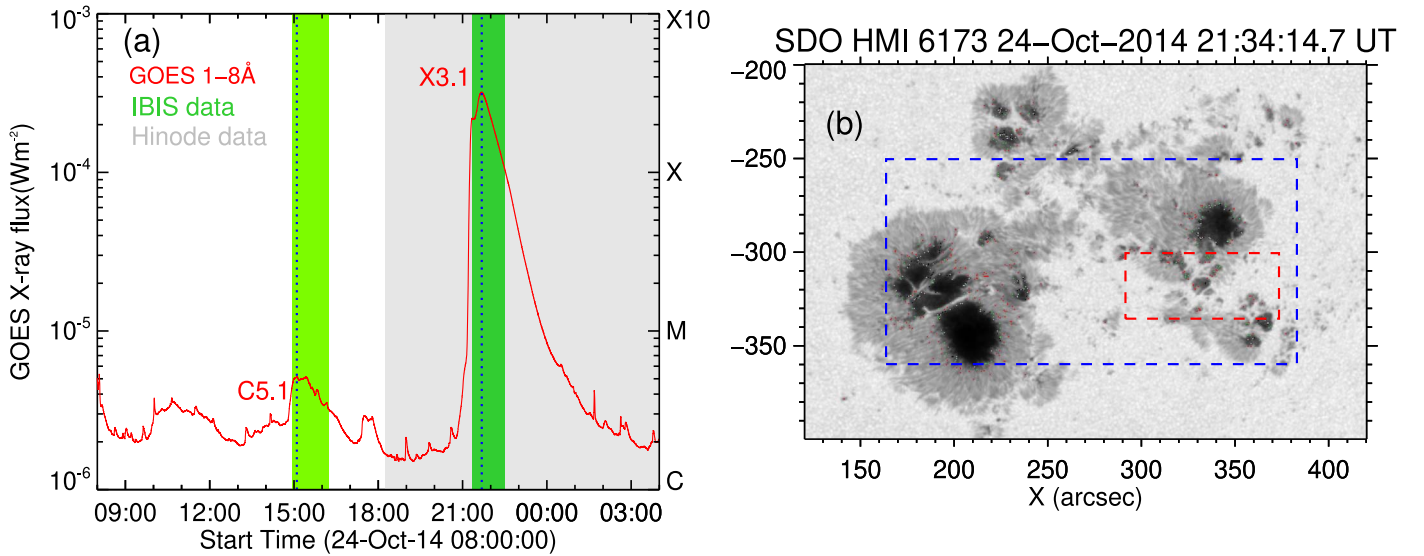
Figure 1. (a) Disk-integrated GOES X-ray flux variations on 2014 October 24. The timeline of data coverage of the IBIS and Hinode instruments is shown by the shaded regions. (b) HMI/SDO continuum image of NOAA AR 12192 taken near the peak time of the X3.1-class flare. The red and blue dashed rectangles indicate the FOVs of the IBIS and Hinode (BFI/SOT) instruments, respectively.

obtained from the Helioseismic and Magnetic Imager (HMI; Schou et al. 2012) on board SDO. Both line-of-sight (LOS) and vector magnetograms (hmi.sharp_cea_720s series) obtained at a cadence of 45 and 720 s, respectively, are used in this study.

The Geostationary Operational Environmental Satellite (GOES) provides the full solar disk-integrated soft X-ray flux used to characterize the magnitude, onset, and peak and end times of the solar flares.

3. Analysis and Results

3.1. Overview of the X3.1 Flare

The X3.1 flare (SOL20141024T 21:41), the strongest flare produced by AR 12192, occurred at the heliographic location of S16W21. The X3.1 flare was not associated with any CME (Sun et al. 2015), similarly to any other X-class flare produced by this AR. The AR evolved into a highly complex region with a Mount Wilson class of $\beta\gamma\delta$ during its flare-prolific period, i.e., 2014 October 20 to 30. On 2014 October 24, AR 12192 possessed multiple inverse S-shaped sigmoidal loops prior to the X3.1 flare. Images acquired by AIA at the 131 and 171 Å wave bands are used to represent the morphological evolution of sheared structures during the X3.1 flare in the first and second row of Figure 2 (flare prior images are not shown). At the start of the X3.1 flare, AR 12192 has multiple sheared structures resembling sigmoids of varying lengths. Two prominent sigmoidal structures are traced by red and blue dashed curves in Figure 2(a). The brightenings in the low-temperature channel of the AIA 171 Å wave band (Figure 2(d)) during the onset of the flare indicate that reconnection occurred in between low-lying sheared loops rooted at the flare ribbons (Figure 2(g)). Figure 2(b) depicts the peak phase of the flare. The flare loops brighten successively from lower to higher atmospheric layers; consequently, plasma gets heated up to 10–20 MK, and an increase in overall brightening is observed. In the decay phase of the flare (Figures 2(c) and (f)), it is evident that many preflare sigmoidal structures (red and blue dashed curves) are still present, and a few more formed as a

result of reconnection (orange dashed curve). Due to the flare reconnection, most of these sigmoidal structures hold the filaments underneath, and these filaments apparently merge to form the long, elongated filamental structure that is shown in Figure 2(i). The bottom row shows the Hα images obtained by GONG, depicting the chromospheric feature evolution during the X3.1 flare at the same epochs as that of the top and middle rows in Figure 2. Motivated by these observations, we studied the dynamics and noneruptiveness of the filamental structures and the mechanisms responsible for them.

3.2. Weak-field Approximation and Changes in B_{LOS}

Under the weak magnetic field limit, the first-order perturbation relates the circular polarization (CP) profile (V) to the first derivative of the intensity profile (I) with respect to wavelength (Landi Degl'Innocenti 1992),

$$V_\lambda = -\Delta\lambda_H \cos\theta \, dI(\lambda)/d\lambda, \quad (1)$$

where the proportionality factor ($\Delta\lambda_H \cos\theta$) depends on the LOS magnetic field, $B_{LOS} = B\cos\theta$, with θ being the angle between the direction of the magnetic field vector and the B_{LOS} component, and the Zeeman splitting is given by

$$\Delta\lambda_H = (e/4\pi m_e c)B\lambda_0^2 g_{eff}, \quad (2)$$

where g_{eff} is the effective Landé factor and has a value of 1.1 for Ca II 8542 Å, B is the magnetic field strength, λ_0 is the central wavelength of the spectral line, e is the charge of an electron, m_e is the mass of an electron, and c is the speed of light.

We determined the chromospheric LOS magnetic field B_{LOS} by computing the slope of the linear regression model fit to V and $-dI(\lambda)/d\lambda$ values obtained for each pixel at all 25 spectral points of the Ca II 8542 Å line acquired by IBIS. We applied the weak-field approximation (WFA) separately to the whole line profile (8539.8–8544.6 Å) and the core (8541.8–8542.2 Å) of the line to obtain two values for B_{LOS}. The B_{LOS} values obtained from WFA applied to the core of the line profile, indicative of the B_{LOS} values at chromospheric height, are used
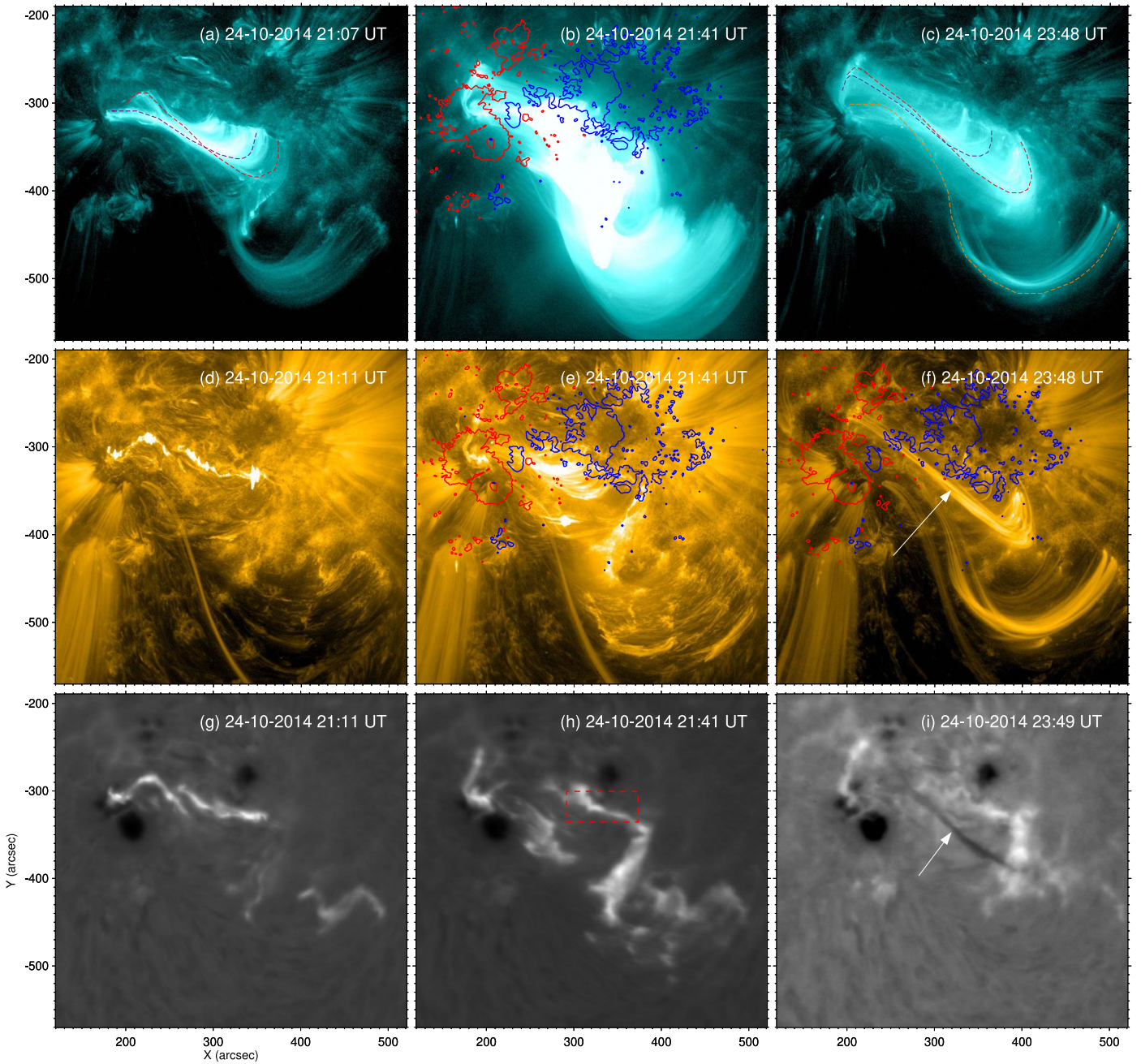
Figure 2. Images acquired by AIA at 131 and 171 Å, as well as Hα images, are used to give an overview of the evolution of AR 12192 during the X3.1 flare. (a)–(c) The AIA 131 Å images show the morphological changes in the multisigmoidal system during the X3.1 flare. (d)–(f) The AIA 171 Å images are at almost the same epochs as the top row, where HMI B_{LOS} maps with contour levels of ±500 G are overlaid. Panel (d) provides evidence of brightenings in the low-lying sheared arcade during the onset of the flare. (g)–(i) GONG Hα images reporting the two-ribbon evolution during the flare and the resultant filament formed underneath the sigmoid, as shown in panel (i). The IBIS FOV is marked by a red dashed rectangle in panel (h).

for further analysis. Kleint (2017) estimated the noise in the polarization images to be 1% of I in 8542 Å, considered pixels having a V signal strength greater than 2% of I in deriving the B_{LOS} value using the WFA method, and found that values less than ±60 Mx cm^{-2} have a low signal-to-noise ratio. However, we have only considered the flare ribbon region for analysis, where the V signal has a strength of about 6%–10% of I (Figure 3). Thus, the uncertainty in the derived chromospheric B_{LOS} values should be less than ±60 Mx cm^{-2}.

Figure 3(a) shows the Stokes I image obtained at the core of the Ca II 8542 Å line by IBIS at 21:32 UT, while the generated chromospheric LOS magnetogram using WFA and the

corresponding photospheric LOS magnetogram obtained from HMI/SDO are displayed in Figures 3(b) and (c), respectively, for qualitative comparison. Though the chromospheric B_{LOS} values obtained from WFA are apparently higher than they are supposed to be, the reconstructed polarity patches are well in agreement with the HMI magnetogram.

To illustrate how well the WFA fits with the observed profile, we considered two arbitrary pixels located in the umbra (green square) and over the flare ribbon (blue square) as shown in Figures 3(a) and (b). The WFA fits for the whole line and core of the line profile (indicated by magenta and blue asterisks, respectively) are overplotted on the observed
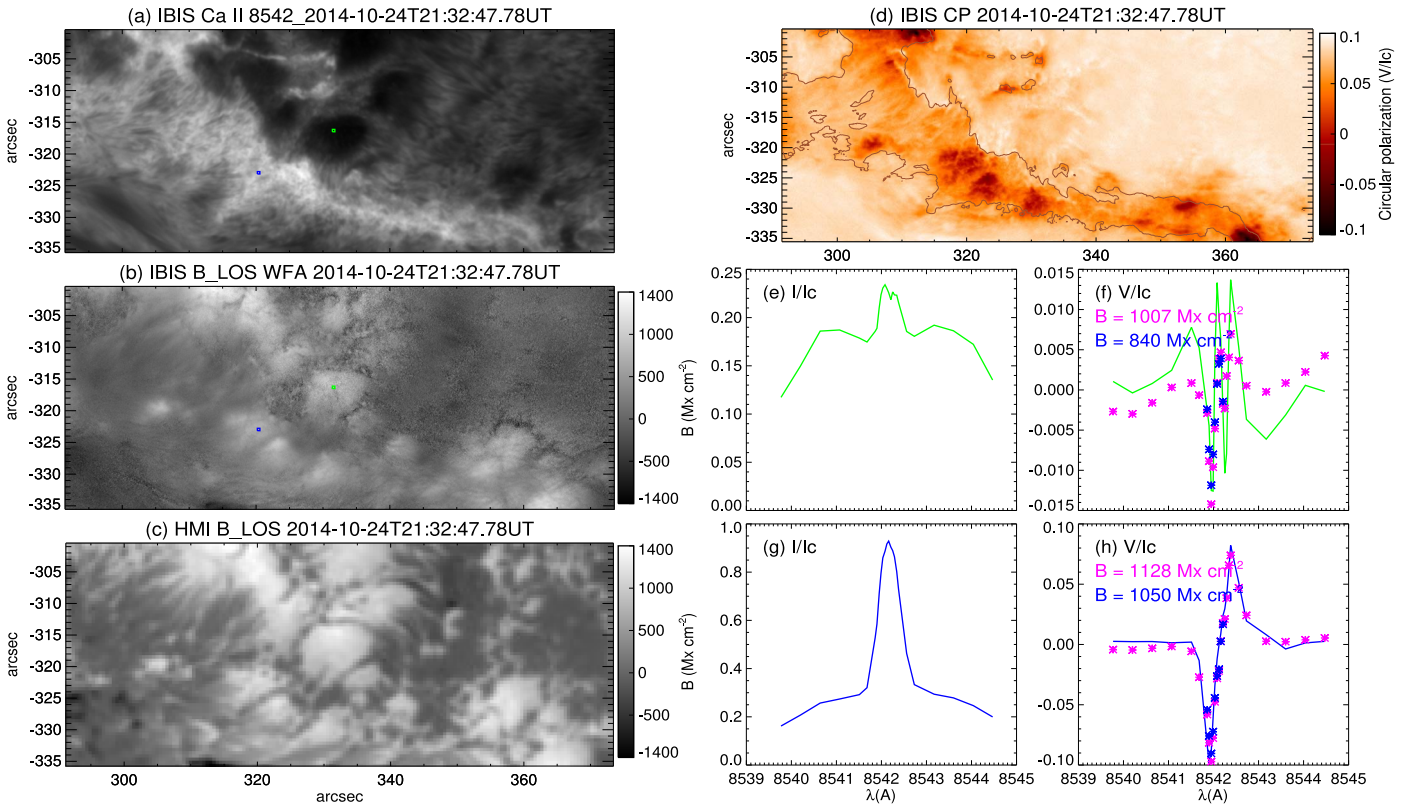
Figure 3. Illustration of the results of WFA using a sample scan obtained by IBIS. (a) Stokes I image obtained at the core of the Ca II 8542 Å line by IBIS. (b) Chromospheric LOS magnetogram deduced by WFA. (c) HMI LOS magnetogram with the same FOV as the IBIS data. (d) CP map obtained from IBIS data. The CP signals are predominant in the flare ribbon (marked by the brown contour), which causes the reconstructed polarity patches within and around the flare ribbon in the chromospheric magnetogram (panel (b)) to have a better match with the HMI magnetogram (panel (c)). (e) Normalized Stokes I profile of an umbral region indicated by the green square in panel (a). (f) V/I profile (solid green line) and the WFA fits obtained from the derivative of Stokes I for the full profile (magenta asterisks) and the core profile only (blue asterisks). (g) and (h) Same as panels (e) and (f) but for a small ribbon region (blue square in panel (a)).

normalized V profile (solid curve) in Figures 3(f) and (h). It is evident in Figure 3(h) that the signal strength of the Stokes V profile and the fitting of WFA with the observed profile is better than in Figure 3(f), indicating that the chromospheric $B_{\rm LOS}$ value obtained in the flare ribbon region has a more reliable estimation (less noise) than in the umbral region. This is true not just for this particular pixel in the flare ribbon but for all of the pixels in the ribbon region, as evidenced in the CP map (Figure 3(d)), where the CP signals are stronger in the flare ribbon region. The mean CP maps were generated using the equation (del Toro Iniesta 2003) CP $= \frac{1}{12 < I_c >} \sum_{i=1}^{12} k V_i$, where $< I_c >$ is the average continuum intensity of the quiet Sun region within the IBIS FOV. With this method, the Stokes V_i images obtained at 12 wavelength positions along the Ca II 8542 Å line are considered such that six wavelength positions are in the blue wing, and the remaining six wavelength positions are from the red wing of the line. To reconstruct the sign of the CP signal, we multiplied the Stokes V_i images in the blue wing with $k = +1$ and the Stokes V_i images in the red wing with $k = -1$.

As all of the twisted field lines in an AR are not related to the flare it produces, Inoue et al. (2016) extensively explored the location of the quasi-separatrix layer (QSL; Demoulin et al. 1996) connected to the X3.1 flare in AR 12192. The QSL is the region with a very high magnetic connectivity gradient that favors the formation of a thin current layer, where the magnetic reconnection is considered to occur relatively easily. Inoue et al. (2016) found that the QSLs of the X3.1 flare correspond

to the boundary of the flare ribbons. The IBIS FOV, indicated by red dashed rectangles in Figures 1(a) and 2(h), encloses a part of the western flare ribbon that corresponds to the location of the QSL (see Figure 6 of Inoue et al. 2016). As the QSLs are potential sites of magnetic reconnection, the evolution of $B_{\rm LOS}$ in different subregions over the flare ribbon during the flare at chromospheric and photospheric heights would be helpful in understanding the orientation and connectivity of the field lines.

The chromospheric $B_{\rm LOS}$, determined from WFA over the IBIS FOV, is studied and compared with the photospheric $B_{\rm LOS}$ obtained from HMI on board SDO. Though the strength of the chromospheric $B_{\rm LOS}$ determined from WFA over the IBIS FOV is found to be higher than the corresponding strength of $B_{\rm LOS}$ at a lower photospheric layer obtained from HMI, the comparison of the behavior of the temporal variation of the $B_{\rm LOS}$ values at these two layers can be studied effectively. Four subregions of 4×4 pixels are selected in different locations over the flare ribbon, outlined by squares of different colors in Figures 4(a) and (f). The average $B_{\rm LOS}$ values of the 4×4 pixels in four different locations are plotted in four different panels for the photosphere and chromosphere separately. We found that $B_{\rm LOS}$ exhibits a decreasing behavior after the flare peak in three subregions at both photospheric (Figures 4(c)–(e)) and chromospheric (Figures 4(h)–(j)) heights. Conversely, in the subregion marked in cyan, $B_{\rm LOS}$ tends to increase (Figures 4(b) and (g)). We would like to note that one of the footpoints of the inverse S-shaped structures (Figures 2(a) and (d)) anchored in
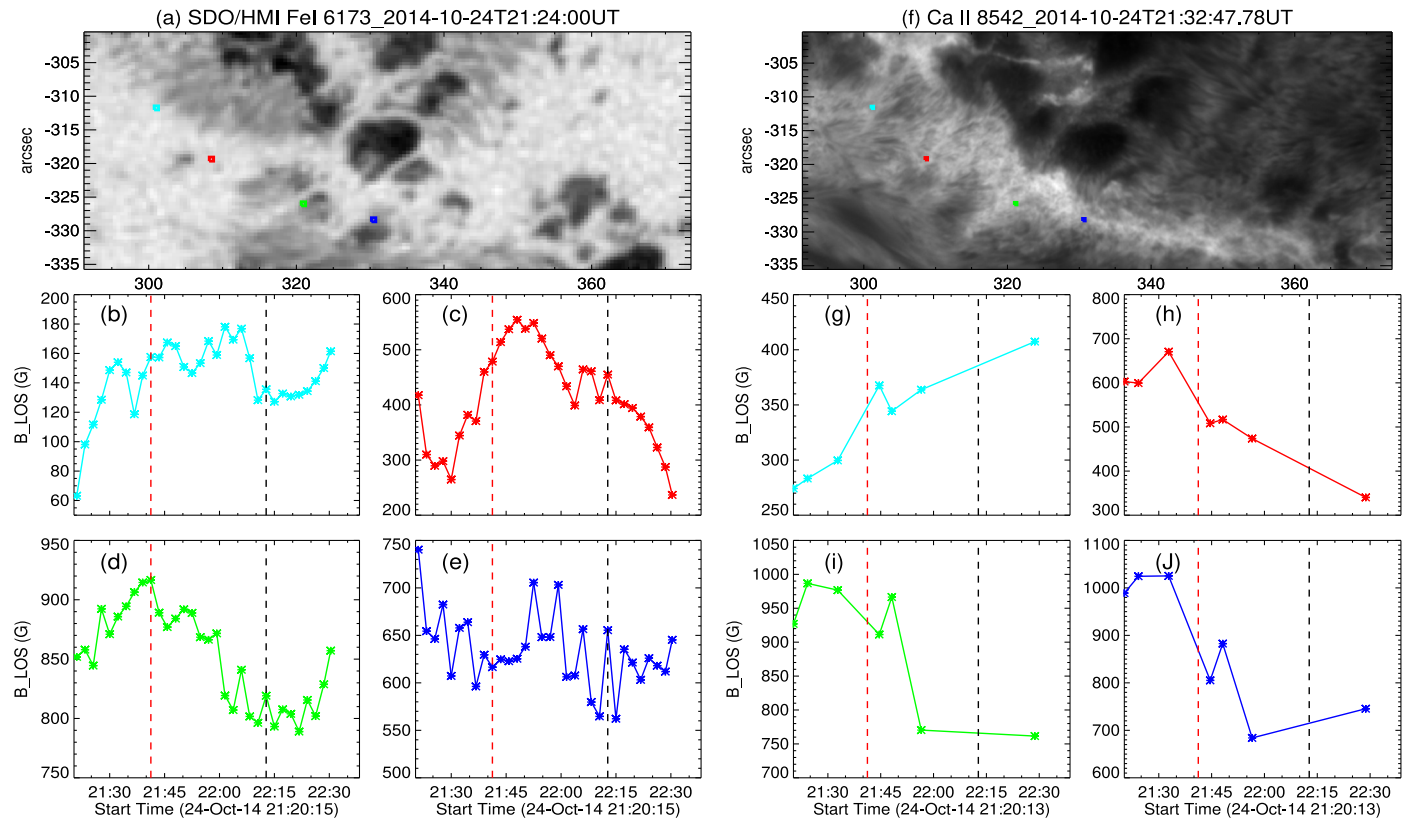
Figure 4. Comparison of the evolution of B_{LOS} values at photospheric (b)–(e) and chromospheric (g)–(j) heights. (a) HMI continuum image with four different locations in the flare ribbon region marked by four different colored squares of 4×4 pixels each. (f) Same as panel (a) but with the Stokes I image of the core Ca II 8542 Å line. The colored curves in all of the remaining panels represent the evolution of B_{LOS} values averaged over the same color of squares indicated in panels (a) and (f). (h)–(j) B_{LOS} at the chromospheric height shows decreasing behavior indicating untwisting of field lines, while corresponding locations at the photospheric height (c)–(e) show an increasing trend. The dashed vertical red and black lines indicate the GOES peak and the end times of the X3.1 flare, respectively.

the western part of the flare ribbon is cospatial with the initial flare brightening regions (yellow filled contours in Figures 5(a) and (e)). The decrease of B_{LOS} in three subregions (lying within the initial flare brightening regions) can be attributed to the untwisting of the field lines due to magnetic reconnection, similar to the scenario described in Figure 8 of Kleint (2017). The more significant decrease of B_{LOS} at the chromosphere height than at the photosphere is mostly due to the fact that the untwisting of the field lines at the higher chromospheric height is more prominent than near the footpoints, i.e., at the photosphere. The different behavior of B_{LOS} in the subregion marked in cyan from other subregions can be understood more clearly by analyzing Figures 5(a) and (e), where this subregion lies outside of the initial flare brightening regions. This indicates that the field lines in this subregion continue to retain a twisted configuration.

3.3. Flux Evolution at the Photosphere and Chromosphere

To compare the temporal evolution of the B_{LOS} flux over the initial flare brightening regions in the photosphere and chromosphere, we used HMI LOS magnetograms and AIA 1600 Å data obtained from SDO with Ca II H and Stokes V/I of Na I D1 line data obtained from Hinode. The Na I D1 V/I data provide the LOS magnetic field distribution in the lower chromosphere just qualitatively. The Na I D1 V/I signal values (dimensionless quantities) are in the range of -1 to $+1$. To obtain the B_{LOS} quantitative distribution, calibration of V/I data with B_{LOS} data obtained from the Hinode SP of SOT has to be

performed (Bamba et al. 2013). We converted the Stokes V/I signal to magnetic field strength in Gauss using the regression line equation, $B_{LOS} = 10900 B_L - 10.21$, which is derived from the scatter plot of Stokes V/I signals and SP B_{LOS} data obtained before the flare onset (20:30–20:50 UT), where B_{LOS} and B_L are the converted LOS magnetic field strength in Gauss and Stokes V/I values, respectively.

In Figures 5(a) and (e), the HMI LOS magnetogram and calibrated V/I map are overlaid with yellow filled contours of the flare brightenings observed during the flare onset in the AIA 1600 Å and Ca II H wave bands, respectively. First, we identified the initial flare brightening regions that are cospatial with the footpoints of the inverse sigmoidal structure (Figure 2(a)), and then regions R1, R2, and R3 (blue squares in Figures 5(a) and (e)) are carefully defined such that they enclose such initial flare brightening regions at both heights. The flux evolution in these three regions at the photospheric and chromospheric heights is shown in Figures 5(b)–(d) and (f)–(h), respectively. At the photospheric height (Figures 5(b)–(d)), the decrease of positive and negative flux is clearly observed during the X3.1 flare in all panels except for region R2, where the positive B_{LOS} flux exhibits an increasing trend from the flare start time. This is possibly due to flux emergence in the positive polarity of R2. Whereas at chromospheric height (Figures 5(f)–(h)), though the B_{LOS} flux evolution trend appears to be the same as that of the photospheric height in these regions, flare-related artifacts are more prominently visible, especially the sudden increase and decrease of positive flux in region R3 (Figure 5(h)). The brightening that appears at the R3
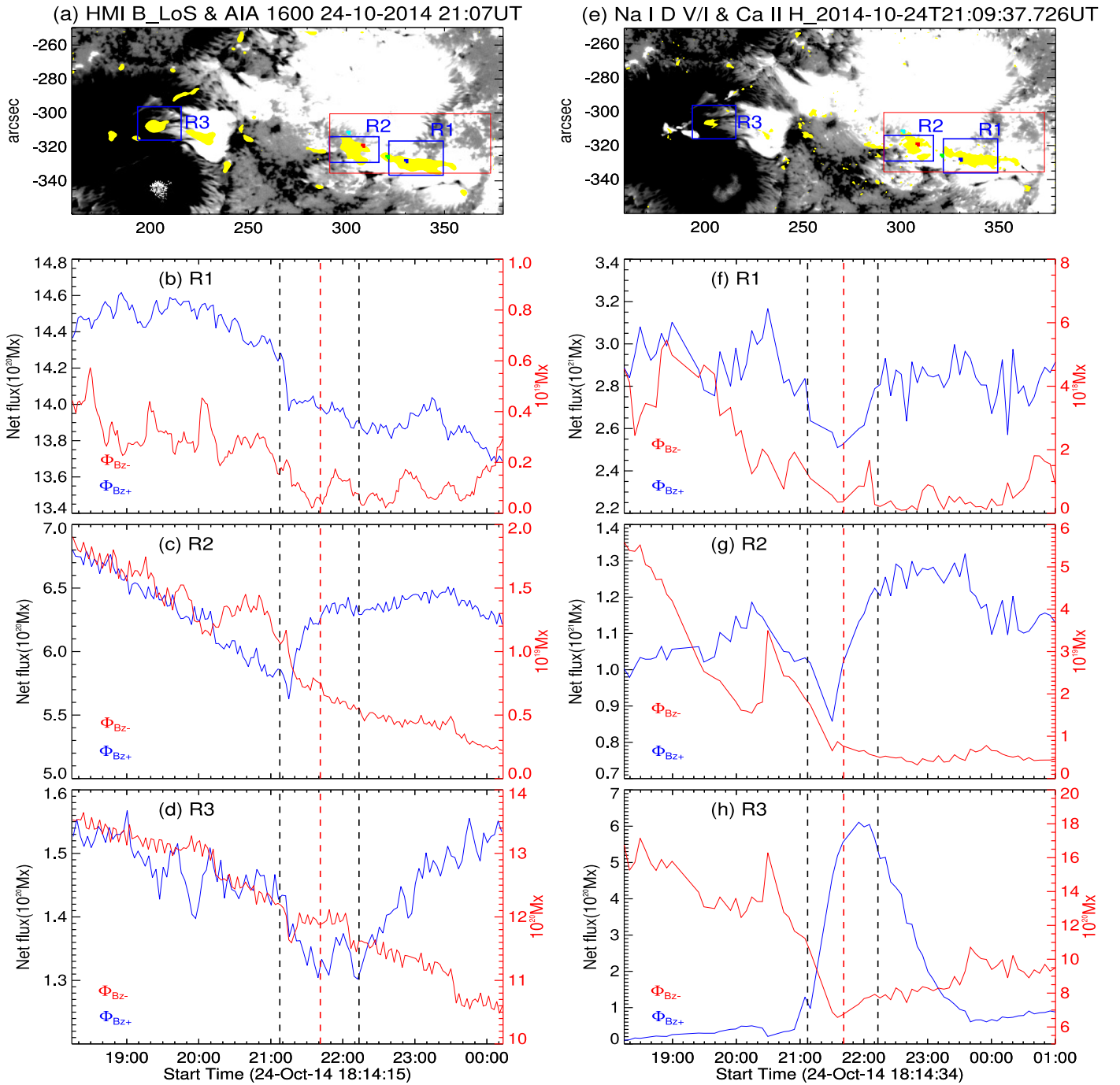
Figure 5. Magnetic flux evolution near the footpoints of the sigmoidal structure in the photosphere (b)–(d) and chromosphere (f)–(h) using HMI and Hinode B_{LOS} data, respectively. (a) HMI LOS magnetogram overlaid with the yellow filled contours of the initial flare brightening observed in the AIA 1600 Å wave band. (e) Na I D1 V/I map overlaid with the yellow filled contours of the initial flare brightening observed in the Ca II H line. The decreasing flux content in the positive (blue solid curves) and negative (red solid curves) polarity patches in the three subregions signifies flux cancellation. The flare artifacts observed in the chromospheric Na I D1 line camouflaged the decreasing trend of net fluxes (panel (h)). The four subregions identified in the IBIS FOV (Figures 4(a) and (f)) are also marked in panels (a) and (e) to specify the location with respect to flare brightening regions. The three dashed vertical lines correspond to the GOES start (black), peak (red), and end (black) times of the X3.1 flare.

region during the peak time of the flare indicates that the Na I D1 line core at the R3 region evidently turned from absorption into emission (Maurya et al. 2012). It is worth noting here that the positive and negative flux ranges at two heights are significantly different, and these values are obtained from two different instruments. Owing to calibration issues, we cannot compare the absolute values of the positive and negative fluxes at two heights, but their decreasing behavior with time at two

heights strongly suggests flux cancellation. The flux cancellation in these brightening regions most likely initiates the tether-cutting reconnection in the sheared arcade, which in turn leads to the X3.1 flare. The brightening of sheared loops rooted at the flare ribbons observed in the low-temperature channel of AIA 171 Å (Figure 2(d)) indicates that the shorter and lower sheared loops undergo tether-cutting reconnection. Figure 2(c) indicates that most of the higher sigmoidal structures continue to exist in
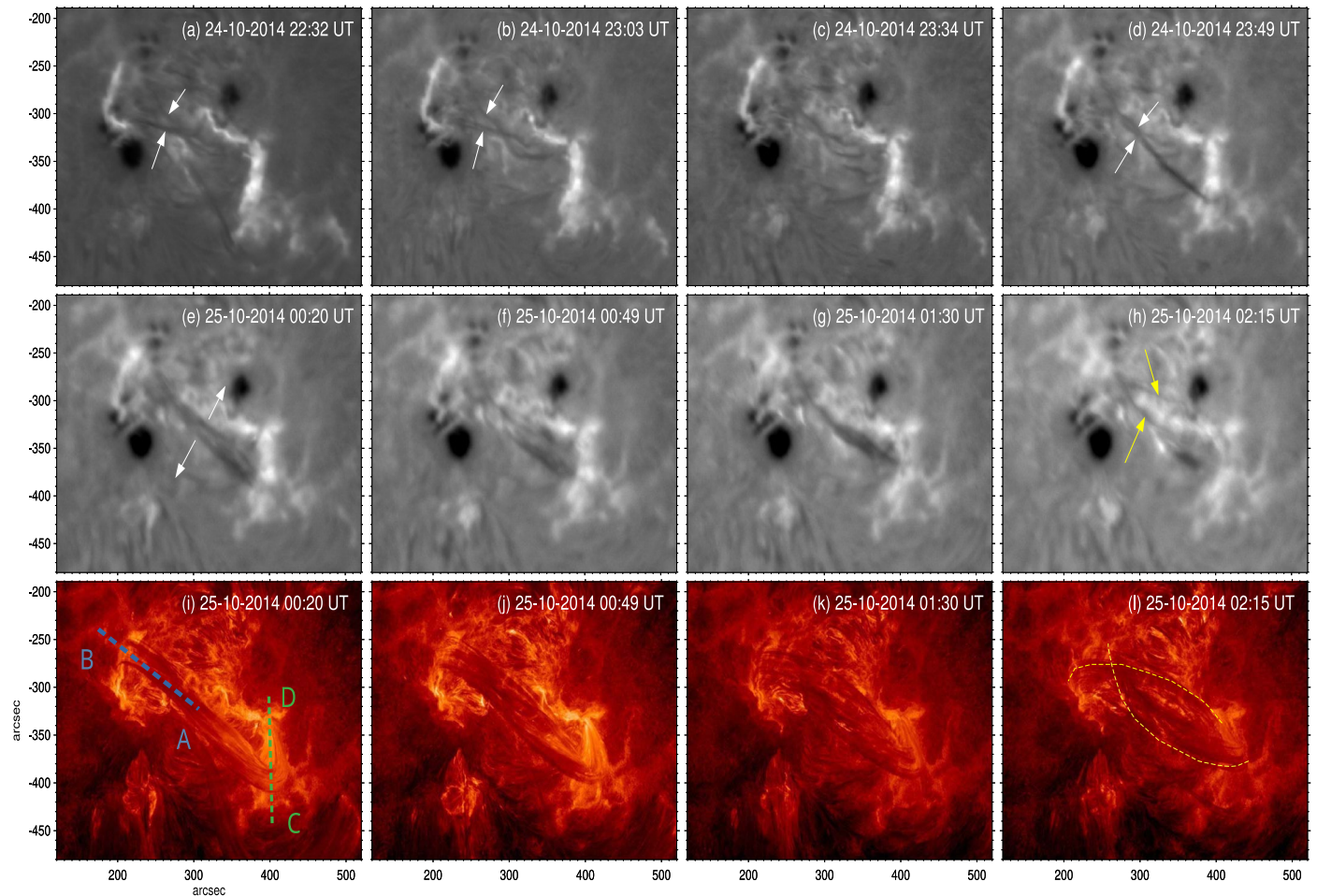
Figure 6. (a)–(d) GONG Hα images showing the merging process of the filaments (underneath the sigmoids) near the PIL region. White arrows are used to guide the visualization of the merging process. (e)–(h) Merged filament splits axially leading to two split filaments are indicated by yellow arrows. (i)–(l) Same as panels (e)–(h) but with AIA 304 Å images, where separated filaments are indicated by yellow dashed curves (panel (l)). An animation of this figure is available, where the AIA 304 Å image sequences run from 20:00 UT on 2014 October 24 to 03:00 UT on 2014 October 25, showing the formation of the sigmoid-filamental structure along the main PIL and the subsequent expansion and separation of the structure. In this figure (static version), the dynamics of the filaments is portrayed only after the flare peak time. In the animated version, the complete evolution of the flaring loops for the entire flare duration of 6–7 hr is shown. The real-time duration of the animation is 30 s.

(An animation of this figure is available.)

their sheared form rather than getting relaxed after the flare. Therefore, it is likely that low-lying sheared structures are involved in the tether-cutting reconnection, leading to the formation of filaments.

3.4. Decay Phase of the Flare

3.4.1. Dynamics of the Filaments

The AR 12192 holds multisigmoidal structures (Figures 2(a)–(c)) on 2014 October 24. These multisigmoidal structures are observed to carry filaments underneath after the peak phase of the flare, and the analysis of the evolution of these filamental structures paves the way to understanding the confinedness of the X3.1 flare. The filaments underlying the multisigmoidal structures lie one above the other, and the evolution of these filaments is displayed in Figure 6 using GONG Hα and AIA 304 Å images.

The panels in Figures 6(a)–(d) report GONG Hα images, showing the merging of filaments (see the white arrows). This process leads to the formation of a merged elongated filament lying over the main PIL (Figure 6(d)). In Figure 6(e), the merged filament starts to undergo separation along its axis. At

this epoch, the merged filament started to rise and expand slowly, and during this process, it underwent separation. What initiates the rising motion of the merged filament will be discussed in Section 3.4.2. In Figure 6(h), the two distinctly separated filaments indicated by yellow arrows are shown. This separation process of the filament is distinctly visible in the AIA 304 Å wave band (Figures 6(i)–(l)) as well, and the separated filaments are marked by yellow dashed curves in Figure 6(l)). Based on the visual inspection, it appears that the coronal loops entered into a more relaxed energy state during the process of separation of the filament.

3.4.2. Emission Measure and Thermal Evolution

The emission measure (EM) and temperature evolution of the sigmoidal structure holding the merged filament underneath is studied by applying differential emission measure (DEM) diagnostic technique to six EUV wave bands of AIA/SDO. The DEM diagnostic technique allows us to measure the amount of emitting plasma along the LOS with respect to temperature. We used a slightly modified version of the DEM reconstruction routine `xrt_dem_iterative2.pro`,

available in Solar Software, which was initially developed for the X-Ray Telescope data of Hinode (Golub et al. 2004; Weber et al. 2004), to work with the AIA data. Nonetheless, Cheng et al. (2012) comprehensively applied this code to AIA data to study the thermal properties of CME structures. Once the DEM (T) maps are reconstructed, the EM and DEM weighted average temperature ($\bar{T}$) can be derived using the following equations:

$$\bar{T} = \int \mathrm{DEM}(T)T dt \Big/ \int \mathrm{DEM}(T) dt,$$
$$\mathrm{EM} = \int \mathrm{DEM}(T) dt, \qquad (3)$$

where integration is performed within the temperature limits of $6.0 < \log T < 7.1$.

The reappearance of the sigmoidal structure (23:30 UT) in the AIA EUV wave bands is cotemporal with the formation of the merged elongated filament in the GONG Hα observations, as shown in Figures 2(f) and 6(d). DEM analysis is used to understand the rising motion and separation of the merged filament. The maps of EM and $\bar{T}$ in the spatial domain are constructed to study the temporal evolution of the thermal and emission properties of the sigmoidal structure during the decay phase of the flare, i.e., from the flare peak time to the GOES X-ray flux attaining the preflare level (October 24 21:41 UT—October 25 02:15 UT). The AIA 171 Å images in the top row of Figure 7 are used to represent the evolution of the sigmoidal structure, while the corresponding maps of EM and $\bar{T}$ are plotted in the middle and bottom rows, respectively. It is evident from Figure 7 that the two footpoints, indicated by two white rectangles of size $25'' \times 50''$, of the sigmoidal structure have different temperatures and EM distributions. The footpoint 1 (FP1) region appears to be at a lower $\bar{T}$ and EM distribution than the footpoint 2 (FP2) region, which has a relatively higher temperature and EM distribution.

To further confirm the asymmetries of these parameters in the two footpoints, we computed the average values of EM and $\bar{T}$ over the two subregions enclosing the footpoints of the sigmoidal structure. The temporal evolution of these parameters is shown in Figures 8(a) and (b). The time period between the reappearance of the sigmoid/formation of the merged filament (October 24 23:40 UT) and the separation of the filament into two distinct filaments until the GOES X-ray flux reaches the preflare level (October 25 02:15 UT) is highlighted by the gray shaded region. During this time period, the average EM and $\bar{T}$ values of FP2 (blue curves) are found to be higher than the average EM and $\bar{T}$ values of FP1 (black curves) in Figures 8(a) and (b).

Once the EM distribution is known, the density (n) of the sigmoidal structure can be obtained using $n = \sqrt{\mathrm{EM}/l}$, where l is the width of the sigmoidal structure. As there are no STEREO observations during 2014 October, the width of the sigmoidal structure is computed directly on AIA 304 Å filtergrams by assuming that the depth of the sigmoidal structure along the LOS is equal to its width. Before the separation of the filament, i.e., at 23:40 UT, the width of the sigmoidal structure near FP1 and FP2 is estimated to be, respectively, 8.7 and 10.8 Mm, and the average EM is 4×10^{28} and 9×10^{28} cm^{-5}, corresponding to densities of 6.7×10^9 and 9×10^9 cm^{-3}, respectively. Once the filaments get separated, i.e., at 2:15 UT, the widths of the sigmoid near FP1 and FP2 increase to 9.9 and 11.7 Mm, and the average EM

reduces to 0.9×10^{28} and 2×10^{28} cm^{-5}, corresponding to a decreased density of 3.1×10^9 and 4.1×10^9 cm^{-3}, respectively. We carried out a similar exercise at the middle of the sigmoid and found that the density decreases from 8.2×10^9 to 2.3×10^9 cm^{-3}. The density of the sigmoid decreases by more than 50% during the process of filament separation. The calculated density values are consistent with past studies (Cheng et al. 2012). These results strongly indicate mass draining or unloading from the sigmoid–filament system.

To compute the velocity of the plasma flow along the filament structure, spacetime or stack plots were generated using the slits AB and CD, as shown in Figure 6(i). The slits AB and CD are placed on the filament to characterize the trajectories of the plasma flows directed toward footpoints FP1 and FP2, and the corresponding spacetime plots are displayed in Figures 8(c) and (d), respectively. Using the trajectories of the plasma flows in the stack plots, projected velocities are computed by taking the time derivative of the smoothed height–time data. It is clear from the stack plots that streaming of plasma along the filament and unloading at its footpoints initiated right after the merging of the filaments, i.e., around 23:45 UT. Initially, the velocity of the plasma flow is slower at FP2 ($\approx$31 km s^{-1}) than at FP1 ($\approx$43 km s^{-1}); this is probably due to density differences between the footpoints, where FP2 is at a higher density than FP1. Gradually, the flow velocity stabilizes and reaches the sigmoid footpoints with an average velocity of $\approx$40 km s^{-1}, which is consistent with past cases (Wang 1999).

We believe that the temperature and density differences between the two footpoints of the sigmoid-filamental structure lead to streaming and counterstreaming of the plasma flow (see the Figure 6 animation) within it, which eventually leads to mass unloading at its footpoints. This draining of mass from the sigmoid-filamental structure would reduce the gravitational force acting on it, helping the subsequent ascent and expansion (Low 1999). However, the sigmoid-filamental structure undergoes splitting instead of eruption, and the two filament sections start to move apart from one another, as shown in Figure 6, due to suppression of overlying fields (see Section 3.5).

3.5. Magnetic Nonpotentiality and Confinedness

As shown in Figure 2(c), after the flare, the AR continues to hold preexisting sigmoidal structures and form new sigmoids. This makes the AR quite different from others; therefore, we decided to further study the temporal evolution of the magnetic nonpotential parameters using HMI vector magnetogram data. Basically, the photospheric magnetic nonpotential measures are area-dependent; hence, we computed the nonpotential parameters by taking into account the minimum flux-imbalance condition ($<4\%$) and the maximum field line connectivity involved in the flare using the AIA EUV images in the flaring area enclosed in the white dashed rectangle in Figure 9(a). The vector magnetic field map corresponding to the area enclosed by the white dashed rectangle is shown in Figure 9(b).

The total absolute magnetic flux, given by $\Phi = \Sigma |B_z| dA$, where B_z is the vertical component of the magnetic field, is computed in positive and negative polarity regions, and their temporal evolution is observed to be almost constant from 20:00 UT October 24 to 02:00 UT October 25 and shown in Figure 9(c). This constant flux on a large scale conceals the flux cancellation occurring in small flare brightening subregions (Figure 5) by averaging out the small-scale flux cancellation
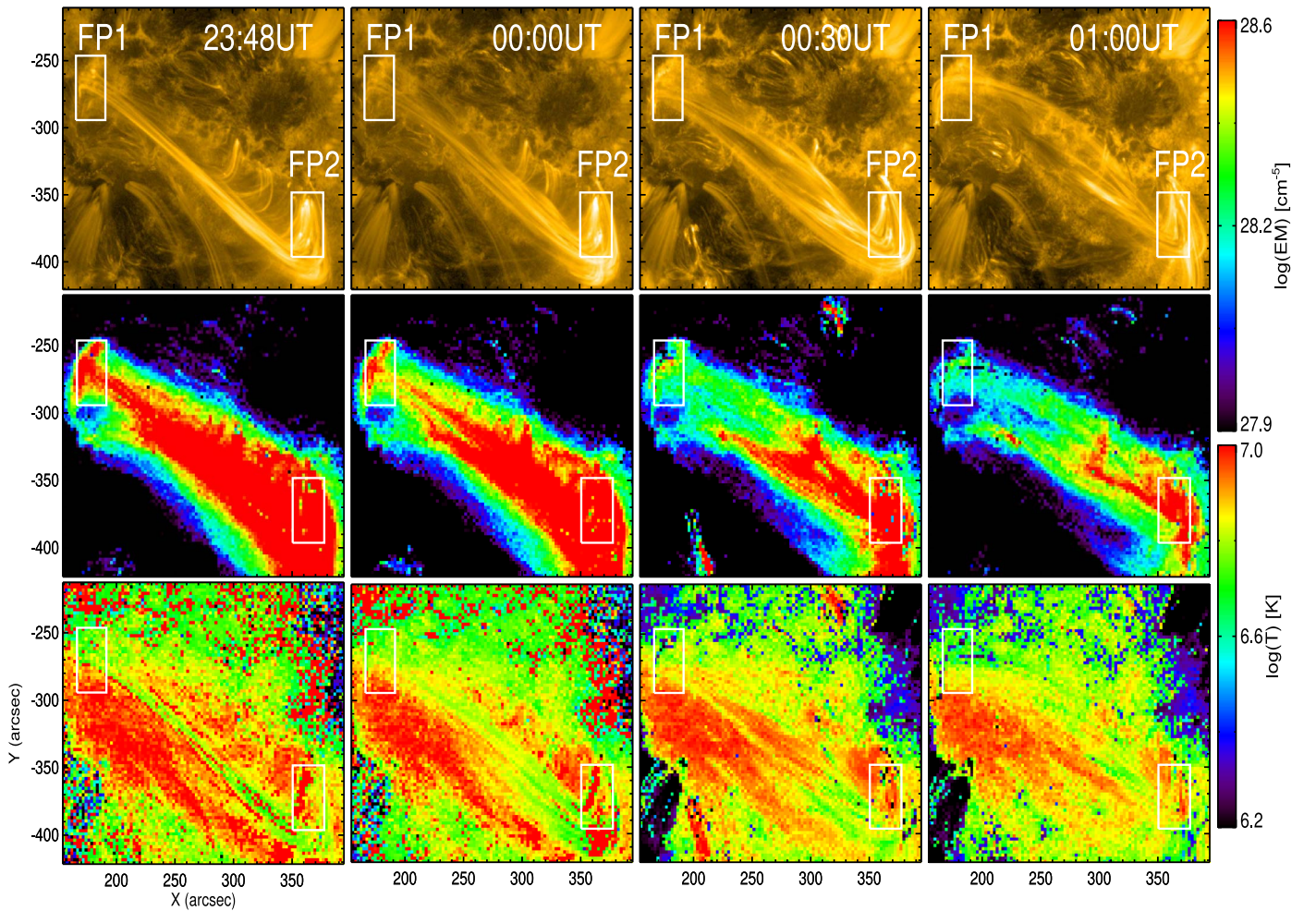
Figure 7. Top row: AIA 171 Å images showing the separation process of the merged sigmoid–filament system. Middle row: maps of the EM distribution at the same epochs as the top row. Bottom row: $\bar{T}$ maps. Clearly, the distribution of $\bar{T}$ and EM is higher around sigmoidal footpoint FP2 than near FP1. The two subregions (white rectangles) of size $25'' \times 50''$ are chosen to study the differences in thermal and emission properties between the two sigmoidal footpoints.

and emergence that occur in small subregions. This indicates that the amount of flux decrease due to the cancellation process occurring at three small flare brightening regions is not enough of a significant decrease to reduce the average flux in a large flaring area. During the time interval of 5–6 hr, the total vertical current in the positive and negative polarity regions of the flaring area, computed using Ampere's law, $I = \sum (\nabla \times B)_z / \mu_o$, also does not show any significant variations (dashed curves in Figure 9(c)). The total unsigned flux (sum of net fluxes) in the flaring area of the X3.1 flare in AR 12192 is about 1.2×10^{23} Mx, which is in agreement with the recent statistical study of Li et al. (2021), showing that flares occurring in ARs with a total unsigned flux greater than 1×10^{23} Mx tend to be confined. Thus, the large absolute flux of AR 12192 could be one of the causes for the confinedness of the X3.1 flare.

Magnetic shear is one of the important parameters that account for the nonpotentiality of the magnetic field during flares. Magnetic shear (Wang et al. 1994) is defined as the product of the observed transverse field strength and the shear angle. The shear angle is the angular separation between the directions of the observed ($\boldsymbol{B}_o$) and potential ($\boldsymbol{B}_p$) vector transverse fields and is given by $\Delta \theta = \cos^{-1}(\boldsymbol{B}_o \cdot \boldsymbol{B}_p / |\boldsymbol{B}_o \boldsymbol{B}_p|)$ (Hagyard & Rabin 1986; Ambastha et al. 1993). The weighted shear angle (WSA) is the ratio of the summation of the magnetic shear to the transverse field strength over all of the

pixels in the flaring area. It is computed by using WSA $= \sum |B_o| \Delta \theta / \sum |B_o|$. The temporal evolution of the average magnetic shear (black solid curve) and WSA (blue dashed curve) of the flaring area is plotted in Figure 9(d). The magnetic shear and WSA clearly exhibit rapid, stepwise enhancements during the onset of the flare and continue to remain in a strong sheared state for more than a couple of hours after the flare. The alignment of the magnetic transverse field vectors (Figure 9(b)) is nearly parallel with the main PIL, further substantiating the increase of the shear in the flaring area in the postflare phase. Again, note that this increase of magnetic shear or WSA during the flare is not due to flux emergence in the flaring area (Figure 9c). In the past, there have been many studies showing the abrupt and irreversible increase of magnetic shear along the flaring PIL regions during major flares. Wang et al. (1994) showed impulsive magnetic shear enhancements along the flaring neutral line during six X-class flares, and Wang et al. (2012) observed the rapid enhancement of magnetic shear in the localized region of the PIL during an X2.2 flare that occurred in NOAA 11158. This is mostly caused by the changes in the photospheric magnetic fields, especially the enhancement of horizontal magnetic fields near the PIL region (Wang et al. 2012; Zuccarello et al. 2020; Vasantharaju et al. 2022), as a consequence of coronal implosion during flares (Hudson et al. 2008). However, the result could be
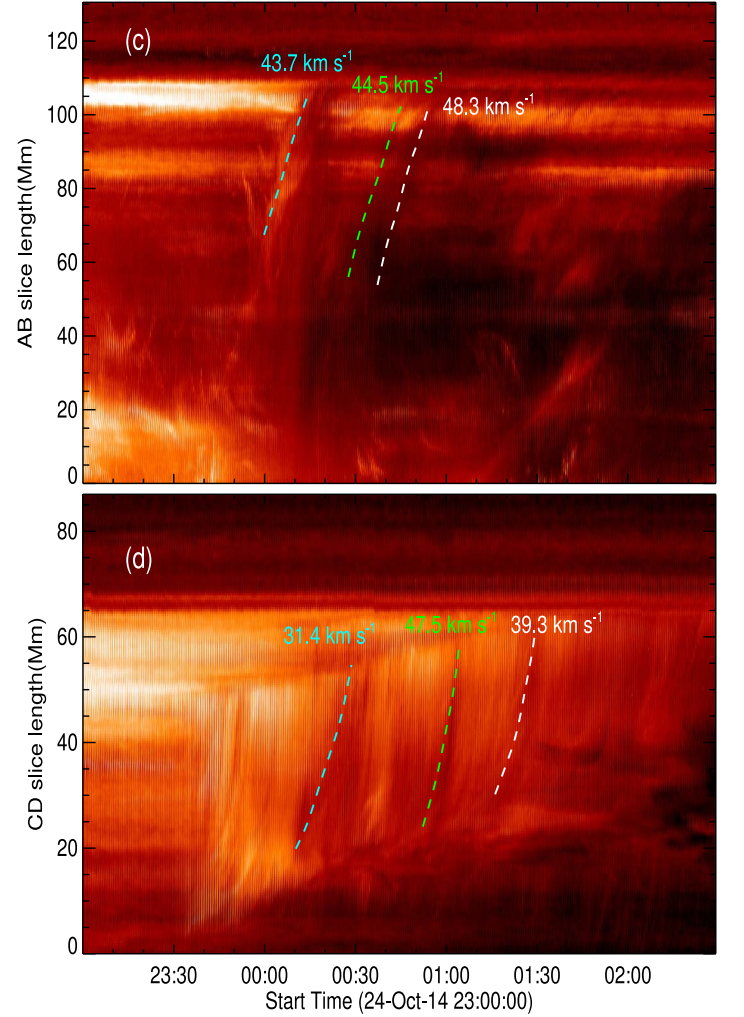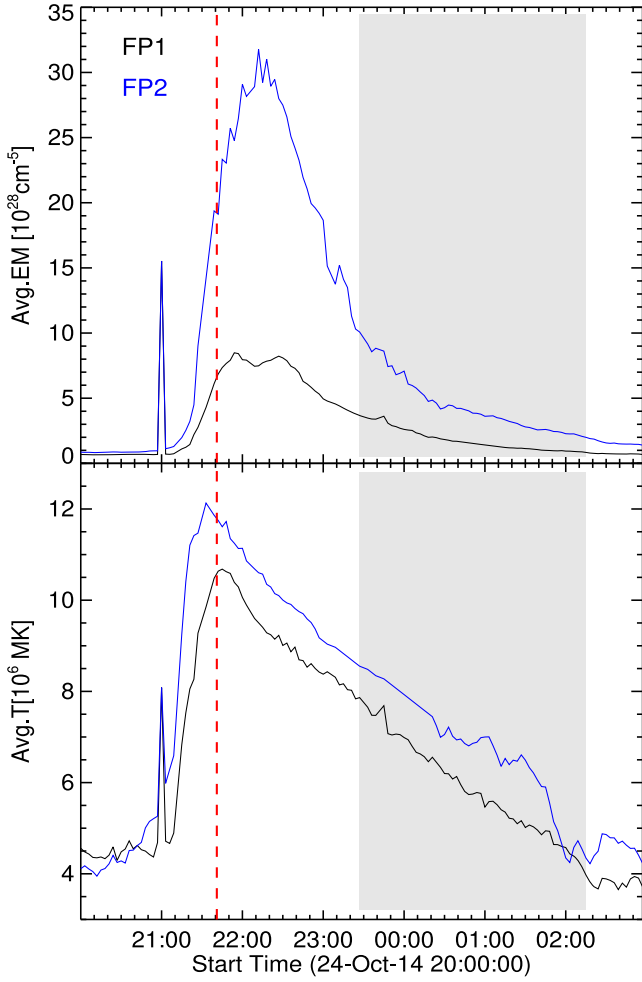
Figure 8. (a) and (b) Temporal evolution of the average EM and $\bar{T}$ of the regions enclosed by white rectangles, shown in Figure 7, near the two footpoints of the sigmoidal structure. Solid black and blue curves refer to footpoints FP1 and FP2, respectively. The dashed vertical red line marks the peak time of the X3.1 flare, and the gray shaded region indicates the time interval of filament separation. (c) Spacetime plot of plasma flow along the AB slice (Figure 6(i)) directed toward FP1 and projected flow velocities are annotated against the trajectories of flows in AB. (d) Same as panel (c) but along the CD slice (Figure 6(i)), showing the flow directed toward FP2.

different if the analysis is extended from localized regions of the PIL to the whole flaring area. For example, Li et al. (2000) considered the whole flaring area in three ARs to study the changes of the average magnetic shear after the flares. They found that the magnetic shear in the flaring area decreases significantly after the flare. On the contrary, we found that the average magnetic shear in the flaring area of AR 12192 increases after the X3.1 flare. This irreversible increase of magnetic shear is consistent with the fact that no observation of eruption is found. If there were any eruptions, they would have taken away magnetic helicity (Nindos & Andrews 2004), thereby leading to less sheared postflare loops. Thus, a permanent increase of magnetic shear is an effect of the confinedness of the X3.1 flare.

Average α ($\alpha_{\rm av}$) or global α is one of the nonpotential parameters used to indicate the degree of twist of the magnetic field lines in an AR. It is derived from the z-component of the magnetic field in force-free conditions ($\mu J_z = \alpha B_z$) and can be computed using the equation given by $\alpha_{\rm av} = \sum [J_z(x, y) B_z(x, y) / |B_z(x, y)|]$ (Pevtsov et al. 1994; Hagino & Sakurai 2004), where B_z is the vertical magnetic field, and J_z is the vertical current density. The temporal evolution of $\alpha_{\rm av}$ is plotted in

Figure 9(e). The $\alpha_{\rm av}$ exhibits a slight increasing trend during the flare and maintains almost the same value for a couple of hours after the flare, indicating that the twistiness of the field lines in the AR slightly increases after the flare, which is in support of the noneruptiveness of the flare. Moreover, the magnetic transverse field vector in Figure 9(b) exhibits a swirling pattern in the upper main negative polarity region; this further corroborates the twistiness present in the field lines. Thus, nondecreasing $\alpha_{\rm av}$ is also a characteristic effect of the confinedness of the X3.1 flare.

Past studies indicate that the magnetic gradient is a better proxy than magnetic shear in locating the occurrence and productivity of flares and their strength in an AR (Wang et al. 2006; Vasantharaju et al. 2018). We therefore computed the strong gradient PIL (SGPIL) using an automated procedure described in Vasantharaju et al. (2018). In this procedure, vertical gradient maps and potential fields are computed using a smoothed B_z map and applying the threshold of the potential transverse field (>300 G) and strong magnetic field gradient (>50 G Mm^{-1}) to the 0 G contours on smoothed B_z maps. The SGPIL length evolution in time is plotted in Figure 9(f). The total SGPIL length decreases from 185 Mm (peak flare) to
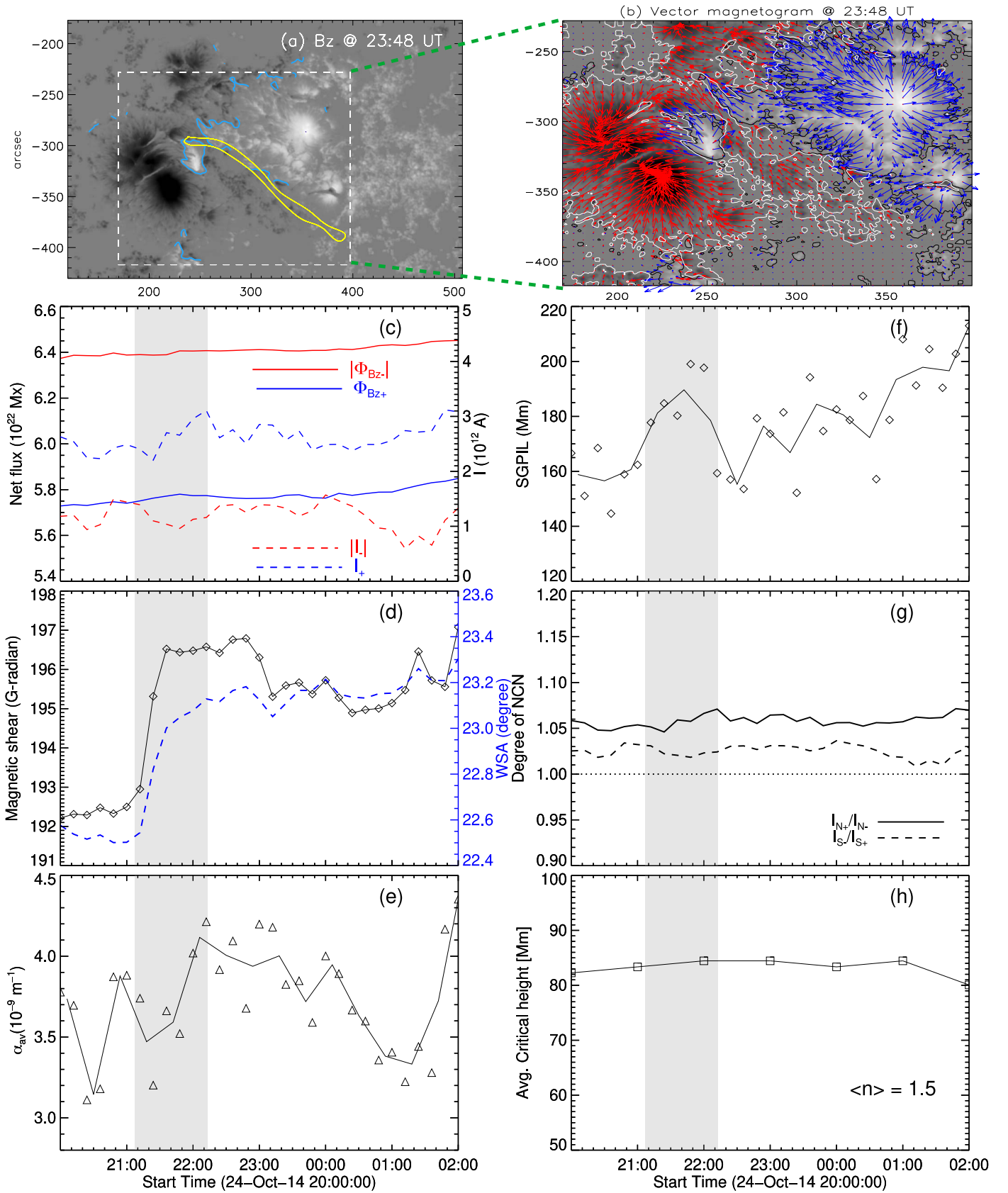
Figure 9. Temporal evolution of magnetic parameters computed within the region enclosed by the white dashed rectangle in panel (a). The automated SGPIL, shown with blue curves, and the contour of the filament (Figure 6(d)), shown in yellow, are overplotted on B_z in panel (a). (b) Vector magnetogram (transverse vectors overlaid on B_z) of the region enclosed by the white dashed rectangle in panel (a). (c) Net flux and current evolution. (d) Stepwise enhancements of magnetic shear and WSA. (e) α_{av} evolution (see text). (f) SGPIL. (g) Degree of NCN signifying full current neutralization (NCN ≈ 1). (h) Average critical heights, when $n = n_c \geqslant 1.5$, over the filament channel. The critical heights are computed every hour for 7 hr. The gray shaded region indicates the time duration of the flare as recorded by GOES. The running average (black solid curve) of the α_{av} and SGPIL measurements is overplotted in panels (f) and (g) to enhance the actual variations.

155 Mm after the flare for only a short time interval. Thereafter, strong gradients near the PIL start to increase, which in turn increases the SGPIL length. The SGPIL segments are fragmented, scattered, and not continuous in the flaring area of AR 12192. Mostly, the twisted flux rope resides above the continuous high gradients of the PIL region, whereas the flaring area in AR 12192 possesses fragmented and scattered SGPILs, which might indicate the AR's inability to host strong, long, and continuous flux ropes capable of eruption (Vemareddy 2019). Thus, fragmented SGPILs in the AR could also be one of the causes of confinedness of the X3.1 flare.

Liu et al. (2017) suggested that the degree of net current neutralization (NCN) would be a better proxy than strong shear or gradients near the PIL in assessing the eruptive nature of flares from an AR. The net current in each polarity has both positive and negative components. The NCN is computed for each polarity by obtaining the ratio of direct current (DC) to return current (RC; Török et al. 2014). The DC and RC are computed by separately integrating the vertical current density values of different signs. The temporal evolution of the |DC/RC| values in both polarity regions is plotted in Figure 9(g). The DC is found to be positive in the north polarity and negative in the south polarity. The |DC/RC| values in both polarity regions are almost equal to unity. Past studies (Liu et al. 2017; Vemareddy 2019) showed that the full current neutralization (NCN = 1) is a characteristic of a noneruptive AR, indicating the absence of DC channels over the PIL region, whereas an AR characterized by nonneutralization (NCN > 1.3) of currents is prone to erupt. Thus, the full current neutralization in AR 12192 for an extended time interval leads to many confined flares, including the X3.1 flare under study.

It is worth noting that the distribution of the fragmented SGPIL in the flaring area and the full current neutralization (NCN = 1), both indicating absence of a robust flux rope along the PIL, may contribute to the confinedness of the X3.1 flare. However, we observed the appearance of sigmoid–filament structure along the main PIL and its dynamics of rise and expansion. Thus, the main contribution to the confinedness of the X3.1 flare should be the stronger inward-directed force from the background field and not the weaker outward-driving force from the inner nonpotential magnetic field. So, we examined the role of the background coronal magnetic field using the potential field solar surface (PFSS; Schrijver & De Rosa 2003) approximation. The lower-boundary data are provided by the HMI vertical component of the magnetic field (SHARP series). The decay index is defined as $n(z) = -\frac{z}{B_h}\frac{\partial B_h}{\partial z}$, where z is the geometrical height from the photospheric surface, and B_h is the horizontal field strength. After the coronal field extrapolation, B_h as a function of z along the filament (yellow contour in Figure 9(a)) is obtained. We repeated the procedure on a time interval of 1 hr from 20:00 UT on October 24 to 02:00 UT on October 25. We then plotted the average decay index along the filament channel and B_h as a function of z at each hour (Figures 10(d)–(f)), and we found that the decay index reaches the theoretical critical value of 1.5 (Török & Kliem 2005) beyond 80 Mm above the surface. The temporal evolution of the average critical height above the filament channel (or main PIL) is plotted in Figure 9(h). Past statistical studies like Baumgartner et al. (2018), Vasantharaju et al. (2018), and Li et al. (2020) showed that the ARs producing confined flares mostly tend to have high critical heights above

50 Mm due to strong confinement, whereas for eruptive flares, the critical heights are less than 42 Mm, indicative of a weaker overlying field strength. For AR 12192 during the X3.1 flare, the almost constant critical height of about 80 Mm throughout the flare duration of 6–7 hr indicates that the background magnetic field strength is strong enough to confine any possible eruption.

Furthermore, Myers et al. (2015) used laboratory experiments to show that the orientation of the external potential field configuration with respect to the flux rope axis is necessary to determine the specific component of the downward Lorentz force. The total potential magnetic field is the superposition of the strapping field, running perpendicular to the flux rope axis, and the guide field, running toroidally along the flux rope axis. The coronal field line rendering extrapolated using PFSS approximation at different time instants throughout the flare duration is shown in Figure 10. Figures 10(a)–(c) display the potential field configuration of AR 12192 at different stages of the X3.1 flare, and panels (d)–(f) show the corresponding variations of the decay index and horizontal magnetic field strength with height. The filament axis lies along the PIL of two main polarities (yellow contour in Figure 9(a)). From the PFSS plots, it appears that the direction of the external poloidal magnetic field is oriented nearly perpendicular to the axial direction of the filament. This indicates that the strapping force is a more dominant downward force than the dynamic tension force, induced by the toroidal field. Thus, we opine that the main contributor to the downward Lorentz force toward confining the X3.1 flare would be the strong strapping field.

4. Summary and Discussion

In this paper, we investigated the nature of the confinedness of an X3.1 flare that originated in AR 12192 in different layers of the solar atmosphere using the multiwavelength observations obtained from ground- (IBIS and GONG) and space-based (Hinode and SDO) instruments. The X3.1 flare (the strongest of the flares produced by AR 12192) was of long duration, lasting for 5–6 hr, and occurred at a heliocentric angle of $\mu = 0.9$. The AR holds multisigmoidal structures prior to the start of the flare. Low-lying sheared field lines underwent tether-cutting reconnection during the flare, bringing minimum morphological changes to the high-lying preflare coronal sigmoidal structures but showing the appearance of filaments underneath these sigmoids. These sigmoid–filament systems lying one over the other exhibit the dynamic behavior of merging and subsequent separation. The temperature and density differences between the footpoints of the merged sigmoid–filament system, as revealed by DEM analysis, aids in understanding the separation and noneruptiveness of the merged filament. The confinedness of the X3.1 flare is mainly caused by the strong confinement provided by the external magnetic field rather than the weaker nonpotentiality of the core AR.

Being located in the southern hemisphere, AR 12192 shows positive helicity and follow the dominant helicity sign rule (Pevtsov et al. 1995), but it shows inverse S-shaped sigmoids on October 24. Generally, inverse S-shaped sigmoids predominantly appear in the northern hemisphere (Rust & Kumar 1996), which makes AR 12192 unconventionally twisted. The EUV/AIA observations reveal that the AR has multisigmoidal structure. Moreover, the brightening of the flare loops with their footpoints rooted at the flare ribbons observed in the low-temperature channel of AIA 171 Å (Figure 2(d))
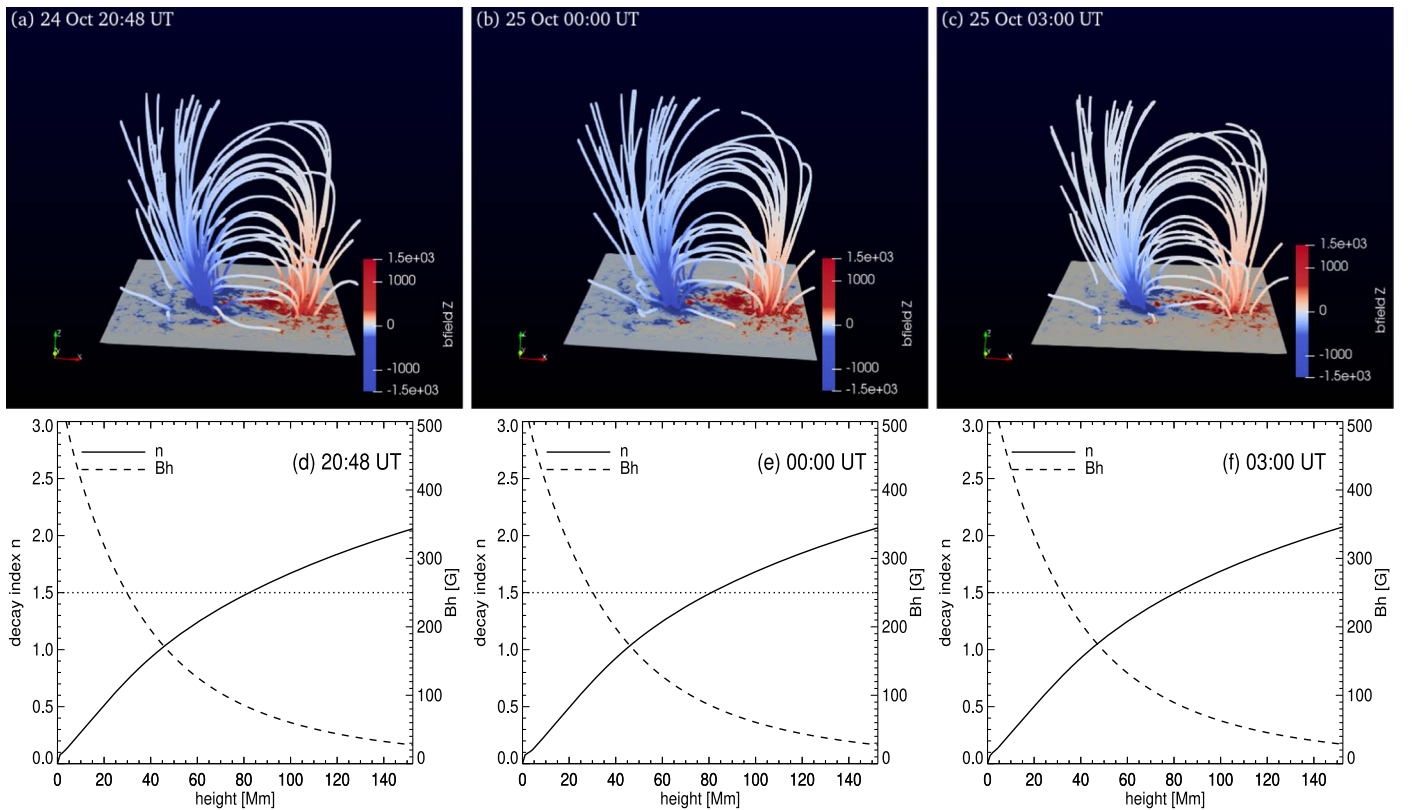
Figure 10. (a)–(c) PFSS configuration of AR 12192 at different time instances, from preflare (20:48 UT) to end (3:00 UT) time, of the X3.1 flare. The unvarying potential field configuration provides the robust confinement throughout the flare. (d)–(f) Corresponding variations of the decay index and horizontal magnetic field strength with height. The decay index, n, reaches 1.5 at about 80 Mm above the photosphere.

provides evidence that the shorter and lower sigmoidal loops undergo magnetic reconnection. The B_{LOS} flux cancellation at both photospheric and chromospheric heights in the brightening regions, which are cospatial with the footpoints of the low-lying sheared field lines, supports the idea of tether-cutting reconnection (Moore et al. 2001) to produce the X3.1 flare and is in agreement with the numerical study of Inoue et al. (2016). Further support of tether-cutting reconnection comes from the analysis of a part of the flare ribbon area (the segment identified as QSL in Inoue et al. 2016), specifically in the initial brightening regions. Using spectropolarimetric data obtained by IBIS to examine the orientation of the field lines during the flare, we found that the scenario resembles the untwisting of field lines during the flare, as observed by Kleint (2017). As the flare progresses, the flare loops successively brighten from lower to higher atmospheric layers (Zhang et al. 2017), and most of the higher sigmoidal structures continue to exist in their sheared form rather than getting relaxed after the flare (Figure 2(c)).

The tether-cutting reconnection in low-lying sheared field lines leads to the formation of filaments near the PIL region (Moore et al. 2001). These filaments, which are underneath the high-lying sigmoids, form the sigmoid–filament systems, which undergo apparent merging to form an elongated filamental structure in the chromosphere, as observed in the GONG Hα images, and are cospatial with an inverse S-shaped sigmoid in the higher layers, as revealed in the EUV/AIA observations. Once the filaments merge together to form a long filament, the sigmoid footpoints are found to have temperature and density differences, as shown by DEM analysis. The temperature and density differences between the sigmoid

footpoints mostly cause the streaming and counterstreaming of plasma inside the filament. The average flow velocity directed toward the footpoints of the filament is found to be about 40 km s^{-1}, in agreement with past studies (Wang 1999), leading to a density decrease of more than 50%. The continuous streaming of the chromospheric material of the filament at its footpoints leads to the draining of the filament mass (see the Figure 6 animation). As the total mass of the filament decreases, the sigmoid holding the filament becomes unstable and consequently starts to rise and expand in an upward direction (Zhang et al. 2021). However, the sigmoid–filament system cannot proceed with its outward motion; instead, it splits axially (Figure 6). We note that the majority of filament eruptions are studied by considering the negligible pressure and mass of the filament plasma suspended by a flux rope in comparison with the dominant magnetic pressure and tension forces of the flux rope and its surroundings (Titov & Démoulin 1999). However, a few studies (Seaton et al. 2011; Jenkins et al. 2018), including this one, provide evidence for "mass unloading" as an eruption driver or increase the height of the flux rope, suggesting that a modification of the gravitational force due to a reduction in mass may influence the stabilization of the flux ropes.

The filaments that are formed in between the flare ribbons along the PIL started to appear in the Hα images around 22:30 UT (Figure 6(a)) only after the flare peak time (i.e., 21:41 UT) but as a result of long flare magnetic reconnection. The AIA/SDO observations revealed the stratified structure of the flare loops, and no set of flare loops underwent significant ascending or descending motions after the flare peak time (Zhang et al. 2017), which is corroborated by observations of no considerable lateral

separation of the flare ribbons (Thalmann et al. 2015). This further substantiates the fact that the same magnetic field structure repeatedly undergoes reconnection for a long period of time, leading to the formation of filaments. Further, the sigmoidal filament structure formed after the flare peak lies along the main PIL with its footpoints rooted at the two flare ribbons on either side of the PIL (see the Figure 6 animation), and the dynamics of filament evolution, like its rising motion and separation, are all closely related to the thermodynamic properties of the same set of flaring loops rooted at the flare ribbons, which all get constrained under the same canopy of the strong external field within the flare duration of 5–6 hr. Thus, we believe that there is an inherent association of the dynamics and noneruptiveness of the filament to the occurrence and confinement nature of the X3.1 flare.

Regarding the causes of the confinedness of the flare, magnetic reconnection in the low-lying, sheared core field is supposed to reduce the constraints of the overlying field lines and allow the core field to erupt (Antiochos et al. 1999; Moore et al. 2001). However, in the present event, the flare loops did not undergo ascending or descending motions after the flare peak time, suggesting that the tether-cutting reconnection failed to weaken the constraints of the upper magnetic loops and produce the eruption of formed filaments. This is not a new result; for example, Zou et al. (2019) studied a confined X2.2 flare that exhibited two episodes of brightening. They found that these brightenings correspond to two magnetic reconnections, one occurring at the null point beside the preexisting flux rope and the other tether-cutting reconnection occurring below the flux rope. However, these two magnetic reconnections failed to produce an eruption because of the strong strapping flux. Thus, although tether-cutting reconnection may act as the trigger of an eruption, it alone is less likely to produce a successful eruption.

In eruptive flares, the ejection of twisted flux ropes into interplanetary space leads to less sheared postflare loops (Forbes & Isenberg 1991). On the other hand, in a confined flare, like the one we have investigated, the twist and shear of the core field are conserved with minimal changes in morphological complexity, as shown in Figures 2 and 9. These are the characteristic effects of the confinedness of the flare. Further investigation of the nonpotentiality of the core of AR 12192 suggests that the AR has fragmented and scattered high-gradient PILs, which is an indication of not having a continuous, strong, twisted flux rope capable of eruption at certain instability conditions (Vemareddy 2019). This, in turn, is in agreement with the full neutralization condition (NCN = 1) of AR 12192, indicating the absence of a DC channel over the PIL. On the contrary, sigmoid–filament structure appeared along the main PIL of the AR and exhibited dynamics of rise and expansion. Thus, the main contribution to the confinedness of the X3.1 flare should be the stronger inward-directed force from the background field and not the weaker outward-driving force from the magnetic nonpotentiality of the core AR.

The AR 12192 had a mean area of more than 3500 millionths of a solar hemisphere (μsh) and a peak area of more than 4000 μsh on October 24 (Cliver et al. 2022) with a total unsigned magnetic flux ($|\phi|$) larger than 1×10^{23} Mx. Recent statistical studies (Li et al. 2020; Cliver et al. 2022) showed that the probability of producing eruptive flares by an AR with an area above ≈ 3500 μsh and $|\phi|$ above 1×10^{23} Mx is greatly reduced. They argued that the larger the flux and area, the

stronger the confinement of the overlying magnetic field. This argument holds true even for the location of the X3.1 flare, which occurs near the center of the AR. Statistically, Baumgartner et al. (2018) showed that confined flares occur close to the AR centers, where the constraining field strength is stronger, and eruptive flares occur at the periphery of ARs, where the confinement is weaker. The total flux and area of the AR along with the location of the X3.1 flare indicate the increase of the horizontal field strength, which decreases the decay rate of the overlying field with height, suppressing eruption. The average critical height (the height at which the decay index = 1.5) above the sigmoid–filament system remains constant at about ≈ 80 Mm throughout the flare duration of 5–6 hr, suggesting the strong confinement over the core of the AR (Baumgartner et al. 2018; Vasantharaju et al. 2018; Li et al. 2020).

It is very difficult to point out the exact component of the downward Lorentz force, generated from the interaction between the external field and the erupting structure, contributing toward confining the eruption with pure observations. Given the fact that the X3.1 flare event is an on-disk event and the nonavailability of STEREO observations, it is difficult to determine the exact height to which the merged filament rose before it actually got suppressed by the downward-acting Lorentz force. However, based on AIA 171 and 304 Å observations (low-temperature channels), the filament eruption is confined in the lower corona (<80 Mm), and the decay index of the external poloidal field does not exceed the criterion for TI (i.e., when $n_c = 1.5$, $H_c = 80$ Mm). Further, the potential field configuration at different time instants throughout the flare duration (Figure 10) provides evidence that the direction of the external poloidal magnetic field is oriented nearly perpendicular to the axial direction of the filament (along the PIL). This indicates that the strapping force is a more dominant downward force than the dynamic tension force, induced by the toroidal field (Myers et al. 2015). However, we cannot rule out the possibility of downward-acting nonaxisymmetry-induced forces due to the radial magnetic field of the MFR carrying the filament (Zhong et al. 2021). The direction of the forces induced by the radial magnetic field of the filament changes with the evolution of the filament, but determining them using the observations is very hard. So, we conclude that from an observational point of view, the confinedness of the X3.1 event is due to the net downward Lorentz force contributed mainly by the strapping field with a possible contribution from the nonaxisymmetry of the filament.

More of such unique X-class confined events need to be analyzed to generalize the results reported in this work and provide reliable input to flare/CME forecasting studies.

ORCID iDs

N. Vasantharaju ⬡ https://orcid.org/0000-0003-2336-5208
F. Zuccarello ⬡ https://orcid.org/0000-0003-1853-2550
S. L. Guglielmino ⬡ https://orcid.org/0000-0002-1837-2262

References

Ambastha, A., Hagyard, M. J., & West, E. A. 1993, SoPh, 148, 277
Andrews, M. D. 2003, SoPh, 218, 261
Antiochos, S. K., DeVore, C. R., & Klimchuk, J. A. 1999, ApJ, 510, 485
Bamba, Y., Kusano, K., Yamamoto, T. T., & Okamoto, T. J. 2013, ApJ, 778, 48
Bateman, G. 1978, MHD Instabilities (Cambridge: MIT Press), 270
Baumgartner, C., Thalmann, J. K., & Veronig, A. M. 2018, ApJ, 853, 105
Cavallini, F., & Reardon, K. 2006, MSAIS, 9, 55
Chen, H., Ma, S., & Zhang, J. 2013, ApJ, 778, 70
Cheng, X., Zhang, J., Ding, M. D., Guo, Y., & Su, J. T. 2011, ApJ, 732, 87
Cheng, X., Zhang, J., Saar, S. H., & Ding, M. D. 2012, ApJ, 761, 62
Cliver, E. W., Pötzi, W., & Veronig, A. M. 2022, ApJ, 938, 136
del Toro Iniesta, J. C. 2003, Introduction to Spectropolarimetry (Cambridge: Cambridge Univ. Press)
Demoulin, P., Henoux, J. C., Priest, E. R., & Mandrini, C. H. 1996, A&A, 308, 643
Feynman, J., & Hundhausen, A. J. 1994, JGR, 99, 8451
Forbes, T. G., & Isenberg, P. A. 1991, ApJ, 373, 294
Golub, L., Deluca, E. E., Sette, A., & Weber, M. 2004, ASP Conf. Ser. 325, The Solar-B Mission and the Forefront of Solar Physics, ed. T. Sakurai & T. Sekii (San Francisco, CA: ASP), 217
Green, L. M., Matthews, S. A., van Driel-Gesztelyi, L., Harra, L. K., & Culhane, J. L. 2002, SoPh, 205, 325
Hagino, M., & Sakurai, T. 2004, PASJ, 56, 831
Hagyard, M. J., & Rabin, D. M. 1986, AdSpR, 6, 7
Harvey, J. W., Bolding, J., Clark, R., et al. 2011, AAS/DPS Meeting, 42, 17.45
Hudson, H. S., Fisher, G. H., & Welsch, B. T. 2008, in ASP Conf. Ser. 383, Flare Energy and Magnetic Field Variations, ed. R. Howe et al. (San Francisco, CA: ASP), 221
Ichimoto, K., Lites, B., Elmore, D., et al. 2008, SoPh, 249, 233
Inoue, S., Hayashi, K., & Kusano, K. 2016, ApJ, 818, 168
Jenkins, J. M., Hopwood, M., Démoulin, P., et al. 2019, ApJ, 873, 49
Jenkins, J. M., Long, D. M., van Driel-Gesztelyi, L., & Carlyle, J. 2018, SoPh, 293, 7
Jiang, C., Wu, S. T., Yurchyshyn, V., et al. 2016, ApJ, 828, 62
Jing, J., Liu, C., Lee, J., et al. 2018, ApJ, 864, 138
Kleint, L. 2017, ApJ, 834, 26
Kliem, B., & Török, T. 2006, PhRvL, 96, 255002
Landi Degl'Innocenti, E. 1992, in Solar Observations: Techniques and Interpretation, ed. F. Sanchez, M. Collados, & M. Vazquez (Cambridge: Cambridge Univ. Press), 71
Lemen, J. R., Title, A. M., Akin, D. J., et al. 2012, SoPh, 275, 17
Li, H., Sakurai, T., Ichimoto, K., & UeNo, S. 2000, PASJ, 52, 483
Li, T., Chen, A., Hou, Y., et al. 2021, ApJL, 917, L29
Li, T., Hou, Y., Yang, S., et al. 2020, ApJ, 900, 128
Liu, R., Titov, V. S., Gou, T., et al. 2014, ApJ, 790, 8
Liu, Y., Sun, X., Török, T., Titov, V. S., & Leake, J. E. 2017, ApJL, 846, L6
Low, B. C. 1999, in AIP Conf. Ser. 471, Solar Wind Nine, ed. S. R. Habbal et al. (Melville, NY: AIP), 109
Maurya, R. A., Vemareddy, P., & Ambastha, A. 2012, ApJ, 747, 134
Moore, R. L., Sterling, A. C., Hudson, H. S., & Lemen, J. R. 2001, ApJ, 552, 833
Myers, C. E., Yamada, M., Ji, H., et al. 2015, Natur, 528, 526
Nindos, A., & Andrews, M. D. 2004, ApJL, 616, L175
Pesnell, W. D., Thompson, B. J., & Chamberlin, P. C. 2012, SoPh, 275, 3
Pevtsov, A. A., Canfield, R. C., & Metcalf, T. R. 1994, ApJL, 425, L117
Pevtsov, A. A., Canfield, R. C., & Metcalf, T. R. 1995, ApJL, 440, L109
Reardon, K. P., & Cavallini, F. 2008, A&A, 481, 897
Rust, D. M., & Kumar, A. 1996, ApJL, 464, L199
Sarkar, R., & Srivastava, N. 2018, SoPh, 293, 16
Schmahl, E. J., Schmelz, J. T., Saba, J. L. R., Strong, K. T., & Kundu, M. R. 1990, ApJ, 358, 654
Schou, J., Scherrer, P. H., Bush, R. I., et al. 2012, SoPh, 275, 229
Schrijver, C. J., & De Rosa, M. L. 2003, SoPh, 212, 165
Schrijver, C. J., De Rosa, M. L., Title, A. M., & Metcalf, T. R. 2005, ApJ, 628, 501
Seaton, D. B., Mierla, M., Berghmans, D., Zhukov, A. N., & Dolla, L. 2011, ApJL, 727, L10
Sun, X., Bobra, M. G., Hoeksema, J. T., et al. 2015, ApJL, 804, L28
Thalmann, J. K., Su, Y., Temmer, M., & Veronig, A. M. 2015, ApJL, 801, L23
Titov, V. S., & Démoulin, P. 1999, A&A, 351, 707
Török, T., & Kliem, B. 2003, A&A, 406, 1043
Török, T., & Kliem, B. 2005, ApJL, 630, L97
Török, T., Kliem, B., & Titov, V. S. 2004, A&A, 413, L27
Török, T., Leake, J. E., Titov, V. S., et al. 2014, ApJL, 782, L10
Tsuneta, S., Ichimoto, K., Katsukawa, Y., et al. 2008, SoPh, 249, 167
van Tend, W., & Kuperus, M. 1978, SoPh, 59, 115
Vasantharaju, N., Vemareddy, P., Ravindra, B., & Doddamani, V. H. 2018, ApJ, 860, 58
Vasantharaju, N., Vemareddy, P., Ravindra, B., & Doddamani, V. H. 2022, ApJ, 927, 86
Vemareddy, P. 2019, MNRAS, 486, 4936
Wang, H., Ewell, M. W., Zirin, J., & Ai, G, H. 1994, ApJ, 424, 436
Wang, H.-M., Song, H., Jing, J., et al. 2006, ChJAA, 6, 477
Wang, S., Liu, C., Liu, R., et al. 2012, ApJL, 745, L17
Wang, Y., & Zhang, J. 2007, ApJ, 665, 1428
Wang, Y. M. 1999, ApJL, 520, L71
Weber, M. A., Deluca, E. E., Golub, L., & Sette, A. L. 2004, in IAU Symp. 223, Multi-Wavelength Investigations of Solar Activity, ed. A. V. Stepanov, E. E. Benevolenskaya, & A. G. Kosovichev (Cambridge: Cambridge Univ. Press), 321
Yashiro, S., Akiyama, S., Gopalswamy, N., & Howard, R. A. 2006, ApJL, 650, L143
Zhang, J., Li, T., & Chen, H. 2017, ApJ, 845, 54
Zhang, Q., Liu, R., Wang, Y., Li, X., & Lyu, S. 2021, ApJ, 921, 172
Zhong, Z., Guo, Y., & Ding, M. D. 2021, NatCo, 12, 2734
Zhou, Z., Cheng, X., Zhang, J., et al. 2019, ApJL, 877, L28
Zirin, H., & Liggett, M. A. 1987, SoPh, 113, 267
Zou, P., Jiang, C., Feng, X., et al. 2019, ApJ, 870, 97
Zuccarello, F., Guglielmino, S. L., Capparelli, V., et al. 2020, ApJ, 889, 65